

Iron fertilization–induced deoxygenation of eastern equatorial Pacific Ocean intermediate waters during the Paleocene–Eocene thermal maximum

Xiaodong Jiang^{1,2,*}, Xiangyu Zhao³, Xiaoming Sun⁴, Andrew P. Roberts⁵, Appy Sluijs⁶, Yu-Min Chou^{2,*}, Weiqi Yao^{2,*}, Jieqi Xing⁷, Weijie Zhang², and Qingsong Liu²

¹School of Environmental Science and Engineering, Guangdong University of Technology, Guangzhou 510006, China

²Department of Ocean Science and Engineering, Southern University of Science and Technology, Shenzhen 518055, China

³School of Oceanography, Shanghai Jiao Tong University, Shanghai 200030, China

⁴School of Marine Science, Sun Yat-Sen University, Zhuhai 519080, China

⁵Research School of Earth Sciences, Australian National University, Canberra, ACT 0200, Australia

⁶Department of Earth Sciences, Utrecht University, Utrecht, 3584 CB, Netherlands

⁷Guangzhou Institute of Geochemistry, Chinese Academy of Sciences, Guangzhou 510640, China

ABSTRACT

The Paleocene–Eocene thermal maximum (PETM), a transient period of global warming, is considered to be an important analog for future greenhouse conditions. It was accompanied by a significant carbon cycle perturbation. Although ocean deoxygenation across the PETM is reported widely, its mechanism in the open ocean remains uncertain. Here, we present magnetic and geochemical analyses of sediments from the eastern equatorial Pacific Ocean. We found that iron fertilization during the PETM by eolian dust and volcanic eruptions fueled eastern equatorial Pacific Ocean productivity. This process led to increased organic matter degradation and oxygen consumption in intermediate waters, leading to deoxygenation. Our findings suggest that iron fertilization could be an important driver of open-ocean oxygen loss, as a side effect of global warming.

INTRODUCTION

Thousands of gigatons (~2500–4500 Gt) of carbon were released into the ocean and atmosphere system over several thousand years during the Paleocene–Eocene thermal maximum (PETM, ca. 56 Ma; Dickens et al., 1997; Zeebe et al., 2016). Environmental changes across this event included rapid global warming by ~3–5 °C (Inglis et al., 2020), intensified weathering (Pogge von Strandmann et al., 2021), hydrological cycling (Carmichael et al., 2017), and ocean deoxygenation (Sluijs et al., 2014). Water-column deoxygenation is invoked as a contributor to oceanic faunal turnover and extinction (Kaiho et al., 1996; Stassen et al., 2015).

Various mechanisms have been proposed as drivers of PETM ocean deoxygenation, including temperature solubility effects, methane oxidation, reduced deep-ocean ventilation, and/or enhanced productivity (e.g., Kaiho et al., 1996; Sluijs et al., 2006; Nicolo et al., 2010; Chang et al., 2018). Along continental margins, at least regionally, high productivity fueled by coastal nutrient inputs potentially enhanced organic matter degradation (reminereralization) and oxygen consumption in the water column and sediments (Sluijs et al., 2006, 2014; Stassen et al., 2015). Although the deep-ocean floors remained oxic (Pälike et al., 2014), geochemical data suggest expanded low-oxygen intermediate water in the Pacific, Indian, and Atlantic Oceans (e.g., Zhou et al., 2014; Yao et al., 2018; Rimmelzwaal et al., 2019).

The eastern equatorial Pacific Ocean (EEPO) was a high-nutrient, low-chlorophyll, iron-limited region over long geological time scales

(Martin et al., 1994). Upwelling and iron fertilization by eolian dust and volcanic ash are both suggested to have stimulated EEPO primary productivity by releasing a critical nutrient limitation (e.g., Winckler et al., 2016; Loveley et al., 2017). This area is, thus, a good target for exploring iron fertilization and upwelling effects on open-ocean productivity and deoxygenation. Total organic carbon (TOC) contents usually fail to constrain open-ocean productivity in ancient records due to degradation. In contrast, degradation of sinking organic matter contributes to enhanced marine barite formation and water-column bacterial metabolism (e.g., Paytan et al., 2007). Thus, sedimentary barite accumulation rates are generally a proxy for export production out of the photic zone (e.g., Paytan et al., 2007; Ma et al., 2014). Biogenic magnetite, the fossilized remains of magnetotactic bacteria (MTB), which generally consist of chains of intracellular nanosized magnetite crystals, is often a good indicator of iron fertilization because MTB growth is controlled by the supply of both organic matter and iron to the seafloor (e.g., Roberts et al., 2011; Wang et al., 2023). Together, marine barite and biogenic magnetite formation in intermediate and bottom waters, respectively, can be used to investigate export productivity from the surface to the deep ocean (Appendix S1 in the Supplemental Material¹).

Here, we combined magnetic measurements, chemical separation, and isotopic analyses of PETM sediments from Ocean Drilling Program

Xiaodong Jiang  <https://orcid.org/0009-0008-0795-0347>

*Corresponding authors: X. Jiang (jiangxd@gdut.edu.cn); Y.M. Chou (chouym@sustech.edu.cn); W. Yao (yaoqw@sustech.edu.cn)

¹Supplemental Material. Appendix S1–S4, Figures S1–S5, and Tables S1 and S2, plus references. Please visit <https://doi.org/10.1130/GEOL.S.25057661> to access the supplemental material; contact editing@geosociety.org with any questions.

CITATION: Jiang, X., et al., 2024, Iron fertilization–induced deoxygenation of eastern equatorial Pacific Ocean intermediate waters during the Paleocene–Eocene thermal maximum: *Geology*, v. 52, p. 276–281, <https://doi.org/10.1130/G51770.1>

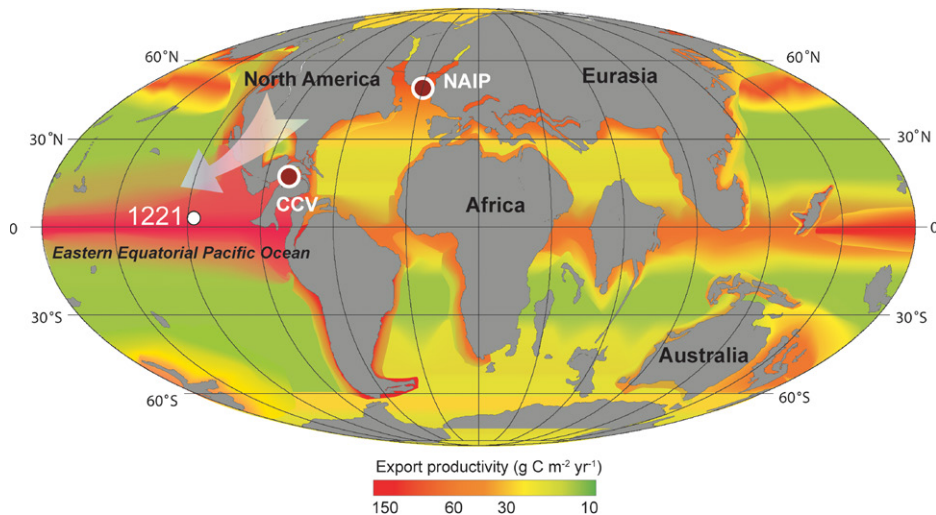


Figure 1. Global export productivity at ca. 56 Ma and location of sediment core from Ocean Drilling Program (ODP) Site 1221C (modified after Ma et al., 2014). NAIP—North Atlantic igneous province; CCV—circum-Caribbean volcanism; white arrow—eolian dust from North America transported to the eastern equatorial Pacific Ocean by trade winds.

(ODP) Site 1221C in the EEPO to investigate the composition and provenance of eolian dust and volcanic products. Marine barite and bio-

genic magnetite were analyzed here to assess links between biogenic productivity and ocean deoxygenation during the PETM.

MATERIALS AND METHODS

ODP Site 1221 Hole C (Fig. 1) was located in the EEPO at a paleowater depth of ~3300 m during the PETM. Paleocene–Eocene boundary beds change up section from yellow dolomite-rich sediments to rose-pink, black, dark brown, and, eventually, tan calcareous ooze in the interval spanned by the most negative benthic foraminiferal carbon isotope ($\delta^{13}\text{C}$) ratios. The coarse ($>38\ \mu\text{m}$) sediment fraction is dominated by benthic foraminifera. We analyzed 26 sediment samples (Table S1) at an average temporal resolution of ~4500 yr based on our age model developed for Hole 1221C (see Appendix S2 [footnote 1]).

Characterization of Biogenic Magnetite and Marine Barite

To characterize biogenic magnetite, magnetic mineral extracts from the sediments were analyzed using a transmission electron microscope (TEM) at the Guangzhou Institute of Geochemistry, Guangzhou, China. Selected area electron diffraction (SAED) was performed using an FEI Titan G2 60-300 TEM. To investigate the morphology and distribution

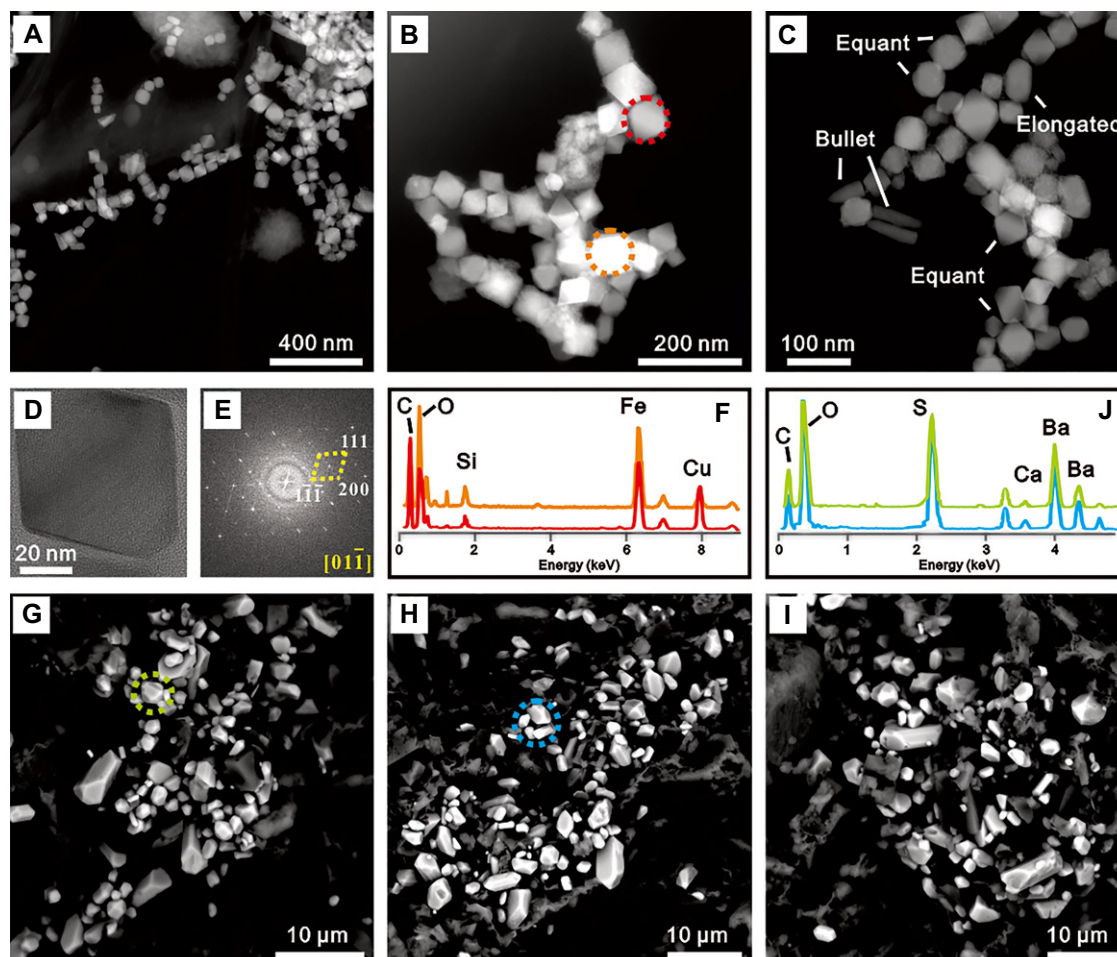


Figure 2. Scanning electron microscope (SEM) and transmission electron microscope (TEM) images of biogenic magnetite and barite. (A–C) Scanning TEM images of magnetofossils. (D–E) High-resolution TEM image and selected area electron diffraction (SAED) patterns; $d(111)$ distances represent lattice spacings along the [011] lattice direction. (F) Energy-dispersive spectroscopy (EDS) results for representative magnetofossils in B and C (Cu peaks originate from TEM grid, and C is from carbon film). (G–I) Images of euhedral barite crystals. (J) EDS results for representative marine barite indicated by colored dashed circles in G and H. Dashed circles are EDS spot locations.

of sedimentary barite, bulk sediments were observed with a scanning electron microscope (SEM) using a Zeiss SIGMA field-emission SEM at the Southern University of Science and Technology (SUSTech), Shenzhen, China.

Magnetic Measurements

To characterize the magnetic properties of PETM sediments, first-order reversal curve (FORC) measurements were made with a 300 ms averaging time using a Lake Shore Cryotronics 8600 vibrating sample magnetometer at SUSTech. An anhysteretic remanent magnetization (ARM) was used to investigate the relative contribution of fine-grained magnetic particles (biogenic magnetite) to the bulk signal (Appendix S1). Two isothermal remanent magnetizations were also applied with a 1 T (IRM_{IT}) forward field and a 0.3 T ($IRM_{0.3T}$) backfield using a pulse magnetizer. The hard isothermal remanent magnetization (HIRM) was calculated as $(IRM_{IT} - IRM_{0.3T})/2$, which was interpreted to represent eolian high-coercivity magnetic mineral inputs (Appendix S2), while the S ratio was calculated as $-IRM_{0.3T}/IRM_{IT}$, which was used to assess low-coercivity mineral contributions to the total magnetic assemblage.

Geochemical Analysis

To explore volcanic eruptions, bulk sediment mercury (Hg) was measured (Appendix S3). To assess the roles of eolian dust and volcanic eruptions, terrestrial material was separated from bulk sediment following a sequential procedure: (1) Carbonate and bioapatite were removed with 1 mol/L HCl at 80 °C for 8 h; (2) organic matter was removed with 30% H_2O_2 at 85 °C for 4 h; and (3) biogenic silica (including diatoms and radiolarians) was removed with 2 mol/L NaOH solution at 85 °C for 4 h. The remaining detrital fraction was rinsed with distilled water three times; and (4) barite was removed at 80 °C for 48 h in a supersaturated Na_2CO_3 solution. Strontium (Sr) and neodymium (Nd) isotope analyses were carried out on the residues to investigate their composition and provenance. Carbonate was removed with 1 mol/L HCl at 40 °C for 8 h; the residues were used to measure major elements for chemical index of alteration (CIA) analyses to assess weathering across the PETM.

RESULTS

Productivity Proxies for Biogenic Magnetite and Marine Barite

The FORC diagrams have an obvious central ridge along the B_c axis (Figs. S1A–S1E), which indicates negligible magnetostatic interactions and the likely presence of intact magnetofossil chains (e.g., Egli et al., 2010; Roberts et al., 2011). TEM observations confirmed the presence of magnetite magnetofossils, with nano-sized chain structures (Figs. 2A–2E), which

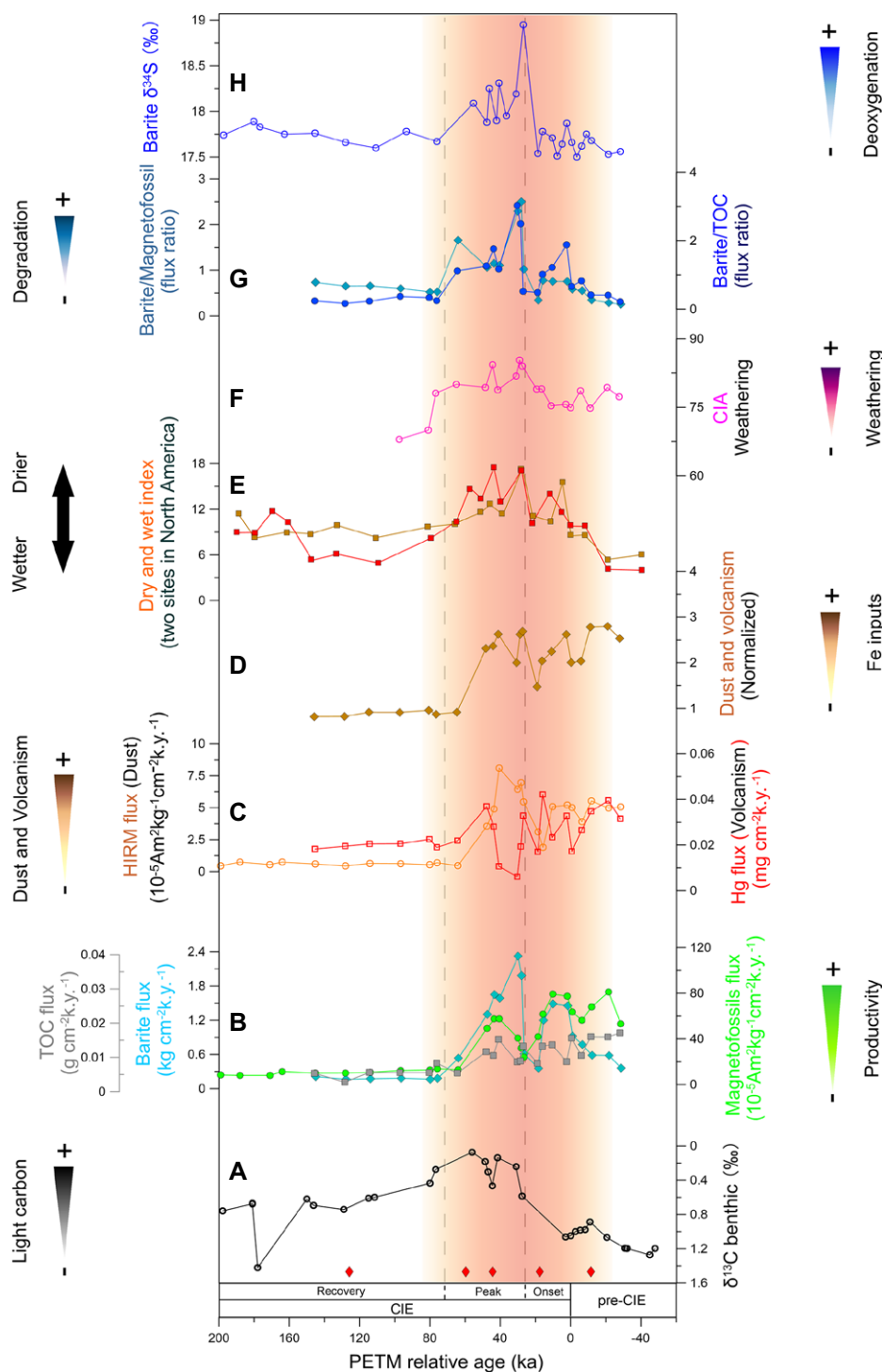


Figure 3. Proxy records across the Paleocene–Eocene thermal maximum (PETM) interval in Ocean Drilling Program Hole 1221C in the eastern equatorial Pacific Ocean. (A) Benthic foraminiferal $\delta^{13}C$ (Nunes and Norris, 2005). (B) Variation of biogenic magnetite and barite flux (Faul and Paytan, 2005) and total organic carbon (TOC) burial (Table S1 [see text footnote 1]). (C) Atmospheric input records. HIRM—hard isothermal remanent magnetization. (D) Normalized Fe input flux from dust and volcanic eruptions. (E) Dry and wet variations in North America (Kraus et al., 2013). (F) Weathering variation proxy of chemical index of alteration (CIA). (G) Flux ratio of barite, biogenic magnetite, and TOC indicating relative water-column organic matter degradation change. (H) Barite $\delta^{34}S$ (oceanic deoxygenation; Yao et al., 2018). Barite flux = (barite [g]/bulk sediment [g]) \times (bulk density [$g\ cm^{-3}$] \times sedimentation rate [$cm\ yr^{-1}$]). Orange shading indicates enhanced dust and volcanic inputs; diamonds indicate sample locations for magnetofossil morphology statistics. CIE—carbon isotope excursion.

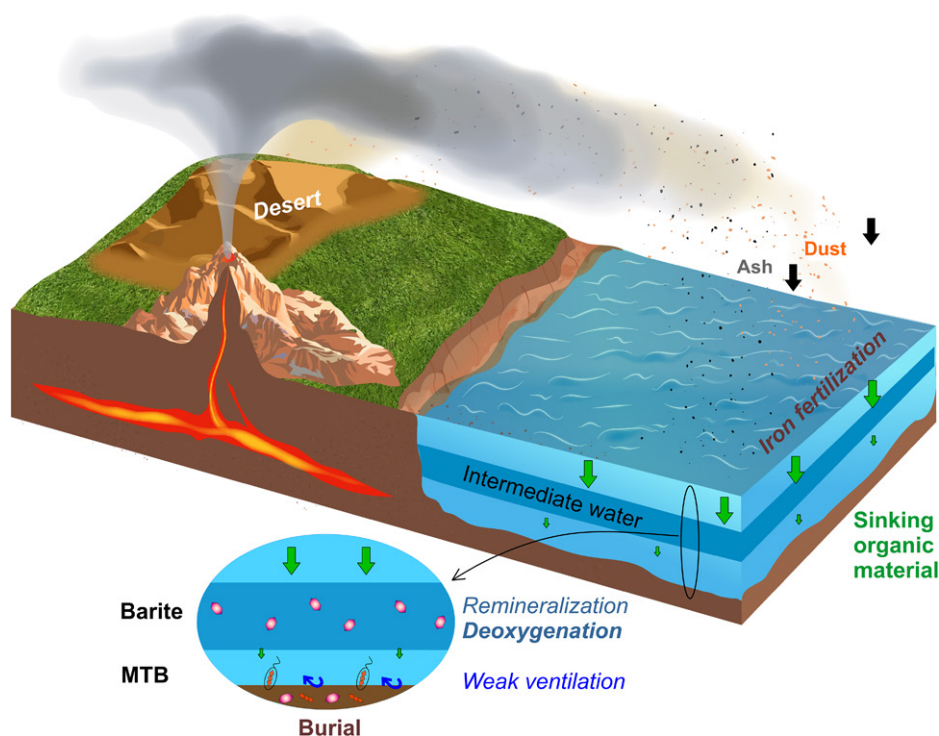


Figure 4. Schematic model of iron fertilization by eolian dust and volcanic eruptions and their contributions to Paleocene–Eocene thermal maximum (PETM) productivity blooms. Organic carbon degradation and remineralization result in intermediate water deoxygenation. Black and green arrows indicate sinking of Fe-rich particles and organic material, respectively. MTB—magnetotactic bacteria.

suggest that biogenic magnetite is the dominant magnetic particle type in the PETM interval (e.g., Chang et al., 2018). The PETM biogenic magnetite particles had dominantly equant morphologies (~80%; Table S2) with minor elongated and bullet-shaped crystals (Figs. 2A–2C). Magnetofossil morphology in marine sediments has been suggested as a paleoenvironmental indicator, with equant crystals dominating in relatively oxidizing conditions (Yamazaki and Kawahata, 1998).

Ubiquitous euhedral barite was observed under SEM (~0.5–10 μm) across the PETM interval (Figs. 2G–2I). Consistent with previous studies (e.g., Yao et al., 2018), the crystal morphology indicates a pelagic origin (Paytan et al., 2007); good preservation quality implies relatively oxic conditions without sedimentary diagenetic alteration. We did not observe detrital barite in our samples, which typically has irregular crystal morphology with coarser sizes compared to marine barite. Marine barite content from the PETM interval (Faul and Paytan, 2005) serves as an export productivity proxy at Site 1221C.

Terrigenous Input and Provenance

Our HIRM and S ratio results indicate minor sedimentary hematite/goethite (Table S1), which is consistent with indications from FORC results showing that the magnetization beyond the narrow central ridge due to coarser and high-

coercivity magnetic particles (Figs. S1A–S1E). Coarse, acicular magnetic particles were also observed under the TEM (Figs. S1F–S1G), which probably have an eolian origin (Appendix S3). An apparent Hg flux spike (Appendix S3) indicates volcanic ash eruption into the EEPO (Fig. S2). Sr and Nd isotope compositions confirm that separate terrigenous components are due mainly to dust and minor volcanic eruptions (Fig. S3).

DISCUSSION

Iron Fertilization in the EEPO

Across the PETM, we observed roughly an eightfold enhanced export productivity from the carbon isotope excursion (CIE) onset to the peak phase, as indicated by marine barite and biogenic magnetite (Figs. 3A–3B). The proportion of net primary productivity exported to the deep ocean drops significantly with ~3 °C warming (Laws et al., 2000), as observed for the PETM in the tropics (Zachos et al., 2003). This implies that the increased biological production must have been large to overcome decreased export efficiency. Although upwelling could have contributed to EEPO productivity (e.g., Winckler et al., 2016), both model simulations and paleo-circulation reconstructions suggest diminished PETM equatorial upwelling and enhanced water stratification (Thomas et al., 2008; Winguth et al., 2012), potentially requiring an alternative mechanism for increased production.

Atmospheric particles can stimulate open-ocean primary productivity. Enhanced eolian dust and volcanism were identified from the CIE onset to its peak, as indicated by HIRM and Hg fluxes (Fig. 3C) and confirmed by Sr and Nd isotope compositions (Figs. S2–S3). Although the Asian continental interior and South America both could have been potential dust sources, our results indicate that eolian dust in the EEPO during the PETM was derived mainly from North America (Appendix S4). Regionally increased hydrological seasonality and prominent dry-wet variations (Fig. 3E) have been documented widely during the PETM (e.g., Bowen and Bowen, 2008; Kraus et al., 2013). This would have facilitated eolian dust production in North America through weathering and erosion (Fig. 3F). North Atlantic igneous province and circum-Caribbean volcanic eruptions during the PETM (e.g., Bralower et al., 1997; Frieling et al., 2016) may have contributed to the EEPO volcanic signal (Appendix S4). Normalized Fe inputs based on dust and volcanic eruption flux correlate well with productivity (Figs. 3B–3D), and a Ba/Fe decrease was observed in periods with enhanced Fe inputs (Fig. S4), so we suggest that iron fertilization by eolian dust and volcanic eruptions from the above sources promoted EEPO productivity across the PETM. These results imply that the EEPO was probably an iron-limited region throughout the Cenozoic, with iron fertilization playing an important role in biogeochemical cycling.

Intermediate Water Ocean Deoxygenation

Enhanced ocean productivity is recorded during the PETM in the EEPO due to iron fertilization. However, the organic carbon (OC) content remained low (~0.01–0.03 wt%; Table S1) compared to that in shelf environments (>2 wt%; Papadomanolaki et al., 2022). A lower increment of seafloor biogenic magnetite flux (indicative of OC export to sediments) was also observed compared to the marine barite flux increase (i.e., export productivity out of the photic zone; Figs. 3B and 3G). These results reflect low OC transmission from intermediate waters to the seafloor despite the relatively productive surface ocean. This is consistent with an insignificant PETM marine increase in OC burial in open-ocean settings (Papadomanolaki et al., 2022). The apparent inconsistency between low TOC content and high primary productivity could be explained by increased OC respiration in intermediate waters. PETM seawater temperatures increased by 4–5 °C, which should have enhanced strongly temperature-dependent (Laws et al., 2000) OC respiration rates and consumed oxygen mostly in intermediate waters. The higher barite-to-TOC ratio (Fig. 3G) is coupled with elevated marine barite S isotope ratios at the same site, which further suggest expanded EEPO intermediate water deoxygen-

ation likely associated with intensified PETM organic matter degradation/remineralization (Figs. 3G–3H; Yao et al., 2018). Our interpretation is also consistent with foraminiferal Cr isotope and I/Ca ratios, which indicate oxygen loss at intermediate ocean water depths (Zhou et al., 2014; Remmelzwaal et al., 2019).

In contrast to EEPO intermediate waters, dominantly equant biogenic magnetite and euhedral marine barite indicate a relatively oxic seafloor environment (Fig. 2; Table S2), consistent with redox-sensitive elements, U isotope evidence, and low OC burial (Pälike et al., 2014; Clarkson et al., 2021; Papadomanolaki et al., 2022). These results suggest that iron fertilization increased surface production with increased export production. Increased OC export led to its intensified remineralization and deoxygenation in intermediate waters but did not lead to an anoxic seafloor or extensive open-ocean OC burial.

Future open-ocean trends project a net primary productivity drop due to intensified stratification and a subsurface oxygen content drop due to stratification and warming (Pörtner, 2019). Our results generally support this scenario but also indicate that iron fertilization might counteract the production drop, albeit at the cost of subsurface oxygenation (Fig. 4). Therefore, our observation is important in the emerging discussion of how global warming will reduce dissolved oxygen in the open ocean and, in turn, affect the marine fishery industry and future food security.

ACKNOWLEDGMENTS

This work was supported financially by the National Natural Science Foundation of China (42274096, 42074071, 92158208, 42261144739, 42274091, and 42376049), the National Key R&D Program of China (2022YFF0802900), the Shenzhen Science and Technology Program (KQTD20170810111725321 and KCXFF20211020174803005), the China Scholarship Council (CSC), the Australian Research Council (DP200100765), the European Research Council (771497), and the Netherlands Earth System Science Center. This research used samples provided by the International Ocean Discovery Program (IODP). We thank the journal reviewers for their constructive and helpful reviews.

REFERENCES CITED

Bowen, G.J., and Bowen, B.B., 2008, Mechanisms of PETM global change constrained by a new record from central Utah: *Geology*, v. 36, p. 379–382, <https://doi.org/10.1130/G24597A.1>.

Bralower, T.J., Thomas, D.J., Zachos, J.C., Hirschmann, M.M., Röhl, U., Sigurdsson, H., Thomas, E., and Whitney, D.L., 1997, High-resolution records of the late Paleocene thermal maximum and circum-Caribbean volcanism: Is there a causal link?: *Geology*, v. 25, p. 963–966, [https://doi.org/10.1130/0091-7613\(1997\)025<0963:HRROTL>2.3.CO;2](https://doi.org/10.1130/0091-7613(1997)025<0963:HRROTL>2.3.CO;2).

Carmichael, M.J., et al., 2017, Hydrological and associated biogeochemical consequences of rapid global warming during the Paleocene-Eocene thermal maximum: *Global and Planetary Change*, v. 157, p. 114–138, <https://doi.org/10.1016/j.gloplacha.2017.07.014>.

Chang, L., Harrison, R.J., Zeng, J.F., Berndt, T.A., Roberts, A.P., Heslop, D., and Zhao, X., 2018, Coupled microbial bloom and oxygenation decline recorded by magnetofossils during the Palaeocene-Eocene thermal maximum: *Nature Communications*, v. 9, 4007, <https://doi.org/10.1038/s41467-018-06472-y>.

Clarkson, M.O., Lenton, T.M., Andersen, M.B., Bagard, M.-L., Dickson, A.J., and Vance, D., 2021, Upper limits on the extent of seafloor anoxia during the PETM from uranium isotopes: *Nature Communications*, v. 12, 399, <https://doi.org/10.1038/s41467-020-20486-5>.

Dickens, G.R., Castillo, M.M., and Walker, J.C., 1997, A blast of gas in the latest Paleocene: Simulating first-order effects of massive dissociation of oceanic methane hydrate: *Geology*, v. 25, p. 259–262, [https://doi.org/10.1130/0091-7613\(1997\)025<0259:ABOGIT>2.3.CO;2](https://doi.org/10.1130/0091-7613(1997)025<0259:ABOGIT>2.3.CO;2).

Egli, R., Chen, A.P., Winkhofer, M., Kodama, K.P., and Horng, C., 2010, Detection of noninteracting single domain particles using first-order reversal curve diagrams: *Geochemistry, Geophysics, Geosystems*, v. 1, 01Z11, <https://doi.org/10.1029/2009GC002916>.

Faul, K.L., and Paytan, A., 2005, Phosphorus and barite concentrations and geochemistry in Site 1221 Paleocene/Eocene boundary sediments, in Wilson, P.A., Lyle, M., and Firth, J.V., eds., *Proceedings of the Ocean Drilling Program, Scientific Results Volume 199: College Station, Texas, Ocean Drilling Program*, p. 1–23, <https://doi.org/10.2973/odp.proc.sr.199.214.2005>.

Frieling, J., Svensen, H.H., Planke, S., Cramwinckel, M.J., Selnes, H., and Sluijs, A., 2016, Thermogenic methane release as a cause for the long duration of the PETM: *Proceedings of the National Academy of Sciences of the United States of America*, v. 113, p. 12,059–12,064, <https://doi.org/10.1073/pnas.1603348113>.

Inglis, G.N., et al., 2020, Global mean surface temperature and climate sensitivity of the early Eocene climatic optimum (EECO), Paleocene-Eocene thermal maximum (PETM), and latest Paleocene: *Climate of the Past*, v. 16, p. 1953–1968, <https://doi.org/10.5194/cp-16-1953-2020>.

Kaiho, K., et al., 1996, Latest Paleocene benthic foraminiferal extinction and environmental changes at Tawanui, New Zealand: *Paleoceanography*, v. 11, p. 447–465, <https://doi.org/10.1029/96PA01021>.

Kraus, M.J., McInerney, F.A., Wing, S.L., Secord, R., Baczynski, A.A., and Bloch, J.I., 2013, Paleohydrologic response to continental warming during the Paleocene-Eocene thermal maximum, Big Horn Basin, Wyoming: *Paleogeography, Paleoclimatology, Paleoenvironment*, v. 370, p. 196–208, <https://doi.org/10.1016/j.paleo.2012.12.008>.

Laws, E.A., Falkowski, P.G., Smith, W.O., Jr., Ducklow, H., and McCarthy, J.J., 2000, Temperature effects on export production in the open ocean: *Global Biogeochemical Cycles*, v. 14, p. 1231–1246, <https://doi.org/10.1029/1999GB001229>.

Loveley, M.R., Marcantonio, F., Wisler, M.M., Hertzberg, J.E., Schmidt, M.W., and Lyle, M., 2017, Millennial-scale iron fertilization of the eastern equatorial Pacific over the past 100,000 years: *Nature Geoscience*, v. 10, p. 760–764, <https://doi.org/10.1038/ngeo3024>.

Ma, Z., Gray, E., Thomas, E., Murphy, B., Zachos, J., and Paytan, A., 2014, Carbon sequestration during the Paleocene-Eocene thermal maximum by an efficient biological pump: *Nature Geoscience*, v. 7, p. 382–388, <https://doi.org/10.1038/ngeo2139>.

Martin, J., et al., 1994, Testing the iron hypothesis in ecosystems of the equatorial Pacific Ocean: *Nature*, v. 371, p. 123–129, <https://doi.org/10.1038/371123a0>.

Nicol, M.J., Dickens, G.R., and Hollis, C.J., 2010, South Pacific intermediate water oxygen depletion at the onset of the Paleocene-Eocene thermal maximum as depicted in New Zealand margin sections: *Paleoceanography*, v. 25, PA4210, <https://doi.org/10.1029/2009PA001904>.

Nunes, F., and Norris, R.D., 2005, Data report: High-resolution stable isotope records across the Paleocene/Eocene boundary, ODP Sites 1220 and 1221, in Wilson, P.A., Lyle, M., and Firth, J.V., eds., *Proceedings of the Ocean Drilling Program, Scientific Results Volume 199: College Station, Texas, Ocean Drilling Program*, p. 1–12, <https://doi.org/10.2973/odp.proc.sr.199.206.2005>.

Pälike, C., Delaney, M.L., and Zachos, J.C., 2014, Deep-sea redox across the Paleocene-Eocene thermal maximum: *Geochemistry, Geophysics, Geosystems*, v. 15, p. 1038–1053, <https://doi.org/10.1002/2013GC005074>.

Papadomanolaki, N.M., Sluijs, A., and Slomp, C.P., 2022, Eutrophication and deoxygenation forcing of marginal marine organic carbon burial during the PETM: *Paleoceanography and Paleoclimatology*, v. 37, <https://doi.org/10.1029/2021PA004232>.

Paytan, A., Averyt, K., Faul, K., Gray, E., and Thomas, E., 2007, Barite accumulation, ocean productivity, and Sr/Ba in barite across the Paleocene-Eocene thermal maximum: *Geology*, v. 35, p. 1139–1142, <https://doi.org/10.1130/G24162A.1>.

Pogge von Strandmann, P.A., Jones, M.T., West, A.J., Murphy, M.J., Stokke, E.W., Tarbuck, G., Wilson, D.J., Pearce, C.R., and Schmidt, D.N., 2021, Lithium isotope evidence for enhanced weathering and erosion during the Paleocene-Eocene thermal maximum: *Science Advances*, v. 7, <https://doi.org/10.1126/sciadv.abh4224>.

Pörtner, H.-O., Roberts, D.C., Masson-Delmotte, V., Zhai, P., Tignor, M., Poloczanska, E., Mintenbeck, K., Alegria, A., Nicolai, M., Okem, A., Petzold, J., Rama, B., and Weyer, N.M., 2019, IPCC Special Report on the Ocean and Cryosphere in a Changing Climate: Cambridge, UK, Cambridge University Press, 755 p., <https://doi.org/10.1017/9781009157964>.

Remmelzwaal, S.R., Dixon, S., Parkinson, I.J., Schmidt, D.N., Monteiro, F.M., Sexton, P., Fehr, M.A., Peacock, C., Donnadiu, Y., and James, R.H., 2019, Investigating ocean deoxygenation during the PETM through the Cr isotopic signature of foraminifera: *Paleoceanography and Paleoclimatology*, v. 34, p. 917–929, <https://doi.org/10.1029/2018PA003372>.

Roberts, A.P., Florindo, F., Villa, G., Chang, L., Jovane, L., Bohaty, S.M., Larrasoana, J.C., Heslop, D., and Fitz Gerald, J.D., 2011, Magnetotactic bacterial abundance in pelagic marine environments is limited by organic carbon flux and availability of dissolved iron: *Earth and Planetary Science Letters*, v. 310, p. 441–452, <https://doi.org/10.1016/j.epsl.2011.08.011>.

Sluijs, A., et al., 2006, Subtropical Arctic Ocean temperatures during the Paleocene/Eocene thermal maximum: *Nature*, v. 441, p. 610–613, <https://doi.org/10.1038/nature04668>.

Sluijs, A., Van Roij, L., Harrington, G.J., Schouten, S., Sessa, J.A., LeVay, L.J., Reichart, G.J., and Slomp, C.P., 2014, Warming, euxinia and sea level rise during the Paleocene–Eocene Thermal Maximum on the Gulf Coastal Plain: Implications for ocean oxygenation and nutrient cycling: *Climate of the Past*, v. 10, no. 4, p. 1421–1439, <https://doi.org/10.5194/cp-10-1421-2014>.

Stassen, P., Thomas, E., and Speijer, R.P., 2015, Paleocene-Eocene thermal maximum environmental

- change in the New Jersey coastal plain: Benthic foraminiferal biotic events: *Marine Micropaleontology*, v. 115, p. 1–23, <https://doi.org/10.1016/j.marmicro.2014.12.001>.
- Thomas, D.J., Lyle, M., Moore, T.C., Jr., and Rea, D.K., 2008, Paleogene deepwater mass composition of the tropical Pacific and implications for thermohaline circulation in a greenhouse world: *Geochemistry, Geophysics, Geosystems*, v. 9, Q02002, <https://doi.org/10.1029/2007GC001748>.
- Wang, D.F., Roberts, A.P., Rohling, E.J., Yao, W., Zhong, Y., Yao, Z., Lu, Y., and Liu, Q., 2023, Equatorial Pacific dust fertilization and source weathering influences on Eocene to Miocene global CO₂ decline: *Communications Earth & Environment*, v. 4, p. 37, <https://doi.org/10.1038/s43247-023-00702-y>.
- Winckler, G., Anderson, R.F., Jaccard, S.L., and Marcantonio, F., 2016, Ocean dynamics, not dust, have controlled equatorial Pacific productivity over the past 500,000 years: *Proceedings of the National Academy of Sciences of the United States of America*, v. 113, p. 6119–6124, <https://doi.org/10.1073/pnas.1600616113>.
- Winguth, A.M., Thomas, E., and Winguth, C., 2012, Global decline in ocean ventilation, oxygenation, and productivity during the Paleocene-Eocene thermal maximum: Implications for the benthic extinction: *Geology*, v. 40, p. 263–266, <https://doi.org/10.1130/G32529.1>.
- Yamazaki, T., and Kawahata, H., 1998, Organic carbon flux controls the morphology of magnetofossils in marine sediments: *Geology*, v. 26, p. 1064–1066, [https://doi.org/10.1130/0091-7613\(1998\)026<1064:OCFCTM>2.3.CO;2](https://doi.org/10.1130/0091-7613(1998)026<1064:OCFCTM>2.3.CO;2).
- Yao, W.Q., Paytan, A., and Wortmann, U.G., 2018, Large-scale ocean deoxygenation during the Paleocene-Eocene thermal maximum: *Science*, v. 361, p. 804–806, <https://doi.org/10.1126/science.aar8658>.
- Zachos, J.C., Wara, M.W., Bohaty, S., Delaney, M.L., Petrizzo, M.R., Brill, A., Bralower, T.J., and Premoli-Silva, I., 2003, A transient rise in tropical sea surface temperature during the Paleocene-Eocene thermal maximum: *Science*, v. 302, p. 1551–1554, <https://doi.org/10.1126/science.1090110>.
- Zeebe, R.E., Ridgwell, A., and Zachos, J.C., 2016, Anthropogenic carbon release rate unprecedented during the past 66 million years: *Nature Geoscience*, v. 9, p. 325–329, <https://doi.org/10.1038/ngeo2681>.
- Zhou, X., Thomas, E., Rickaby, R.E., Winguth, A.M., and Lu, Z., 2014, I/Ca evidence for upper ocean deoxygenation during the PETM: *Paleoceanography*, v. 29, p. 964–975, <https://doi.org/10.1002/2014PA002702>.

Printed in the USA